Supplementary Information (SI) for Journal of Materials Chemistry A.

Supplementary information:

Rapid Lithium Extraction via Solar Thermal Interfacial Evaporation with Zero Liquid Discharge

Luheng Tang, Subhash C. Singh*, Mingjiang Ma, and Chunlei Guo*
The Institute of Optics, University of Rochester, Rochester, NY-14627, USA
*Corresponding author: ssingh49@ur.rochester.edu, guo@optics.rochester.edu

Supplementary Note 1

Superwicking Black Metal (SWBM) surface fabrication and characterizations

Experimental setup for the fabrication of the SWBM surface is described in **Fig. S1a**. The femtosecond laser beam (Ti: Sapphire, Coherent Astrella) operates at 800 nm wavelength, 780 µJ/pulse energy and 1 kHz repletion rate. The 300/2000 µm thickness titanium foil is mounted on an XY translation stage and the laser beam is focused on the target surface using a planoconvex lens and scans line-by-line with a scan speed of 1 mm/s.

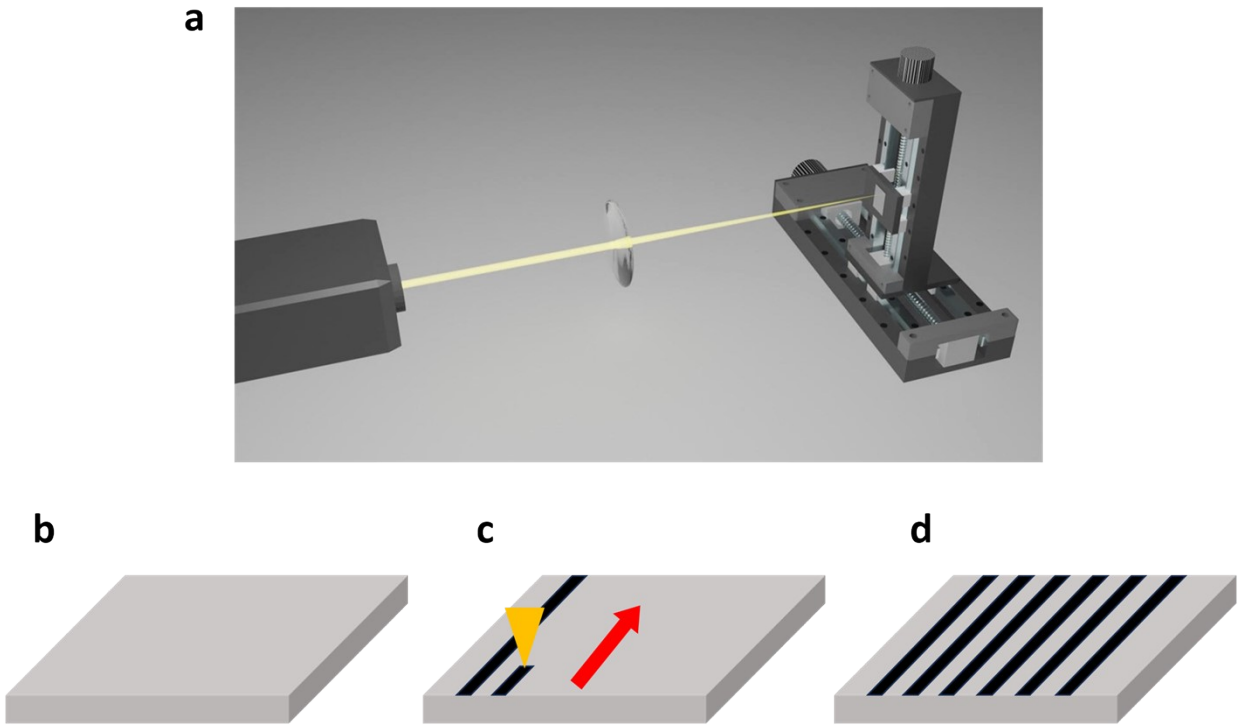

Figure S1: (a) Schematic of laser fabrication of the SWBM. (b-d) Schematic of laser processing: b) unprocessed sample, c) processing, d) processed. The yellow arrow represents laser and red arrow represents the direction of laser processing, the grey color cubic represents passive titanium foil and black stripe represents the laser treated region.

Supplementary Note 2

SWBM Surface topography measurements using 3D laser confocal microscope

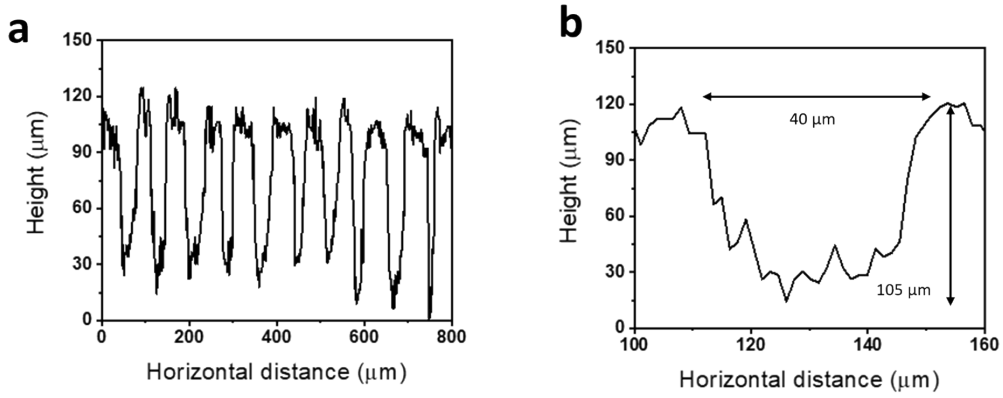

Figure S2: a) Depth profile of the SWBM using 1.5W. The average depth of the micro-capillary is 105 μm. b) An enlarge view of one representative micro-capillary of SWBM. The width of the micro-capillary is approximately 40 μm.

Supplementary Note 3

HTO deposition method on SWBM surface

These LTO nanoparticles are initially uniformly dispersed in the water at 60 C. Subsequently, the solution with LTO is deposited on the SWBM heated at 60 C. Finally, the solvent evaporates, leaving LTO coated on the micro grooves of the SWBM. To extract the lithium ions, the SWBM with LTO is immersed in the HCL solution (0.25 mol/L) for 24 hours at 60 C. After that, the sample is washed by deionized water and ethanol for several times and dries at 60 C for 2 hours. These process turns LTO to HTO for recyclable lithium ion harvesting.

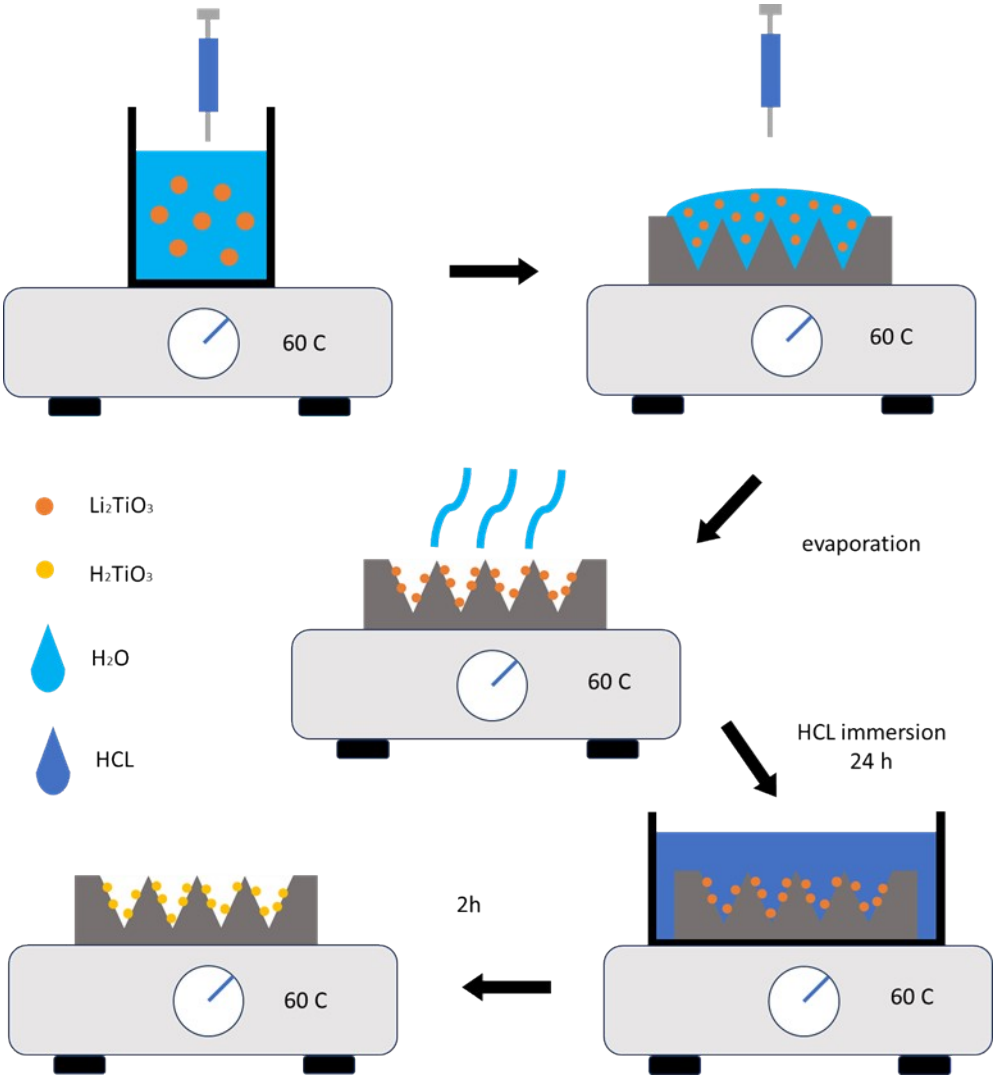

Figure S3a: Diagram describing the process of HTO deposition on SWBM surface.

HTO deposition uniformity analysis

To evaluate the uniformity of deposition, microscope image is taken at different location of the STEEL. Then, for each image, we use image processing code to distinguish the HTO nanoparticles, highlight it with the red color and calculate the percentage coverage. The result shows that the coverage is basically uniform around 40%.

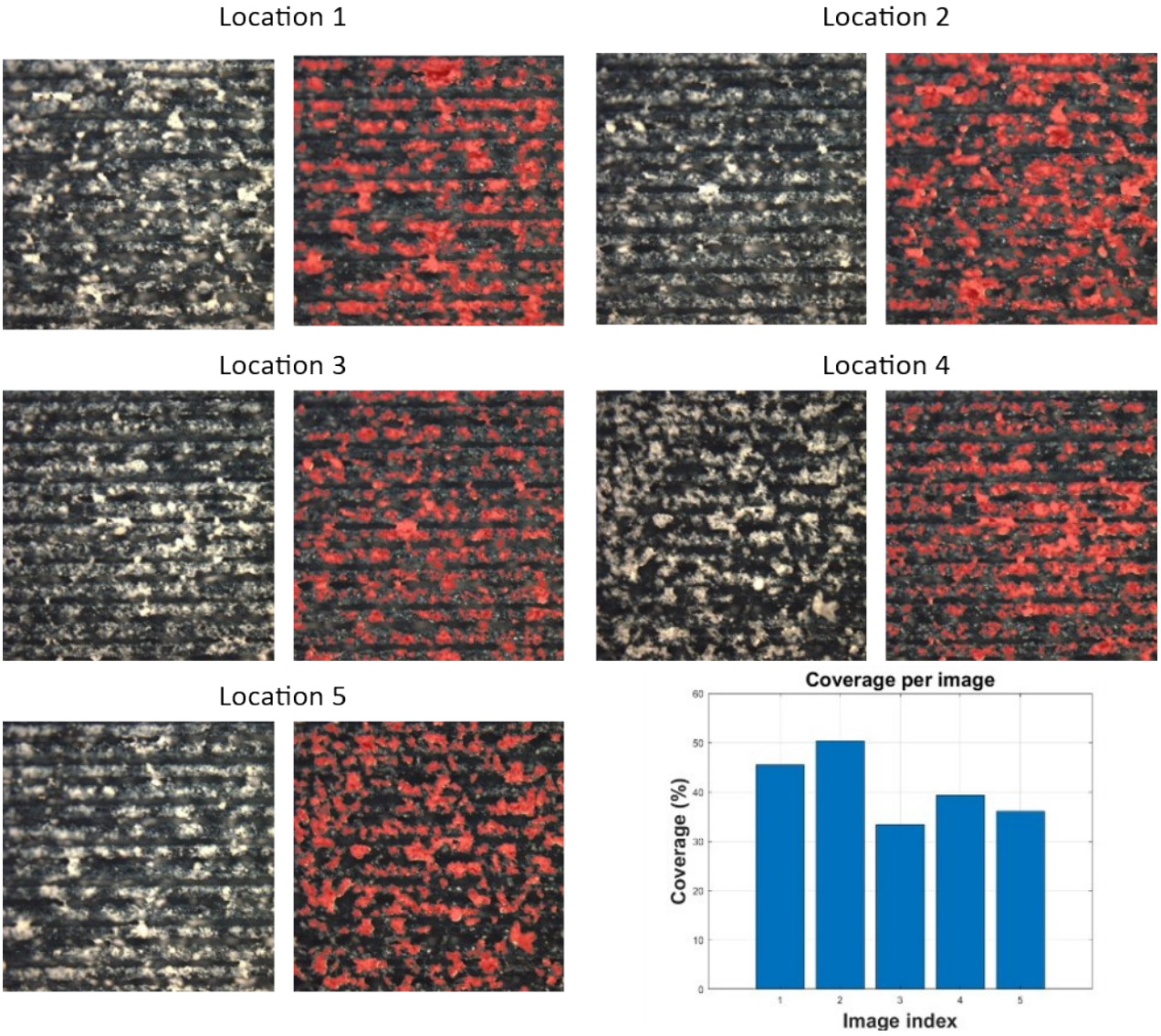

Figure S3b: image of different location of the STEEL showing HTO deposition. Image processing is used to distinguish the HTO nanoparticles, highlight it with red color and count the percentage coverage.

Characterization of STEEL and L-SWBM

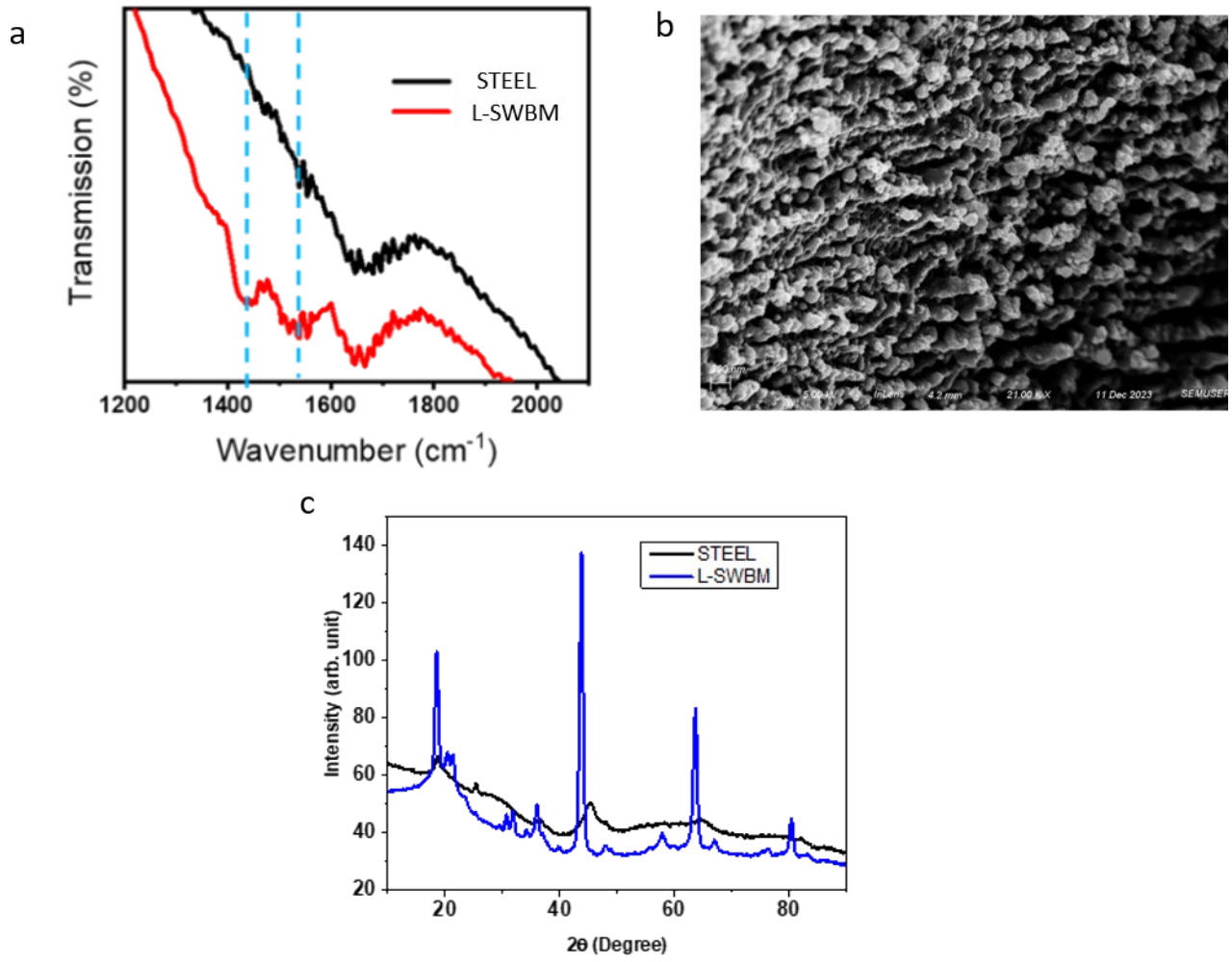

Figure S4: a) FTIR spectra for the LTO covered SWBM and HTO functionalized SWBM. The blue dotted lines mark the missing peak around 1435 cm^{-1} and 1520 cm^{-1} in the HTO functionalized SWBM sample produced after the acid treatment. b) SEM image of HTO nanoparticles depositing in the microgrooves. XRD spectra of c) L-SWBM and d) STEEL.

Supplementary Note 4

Experimental measurement of wicking dynamics of SWBM samples

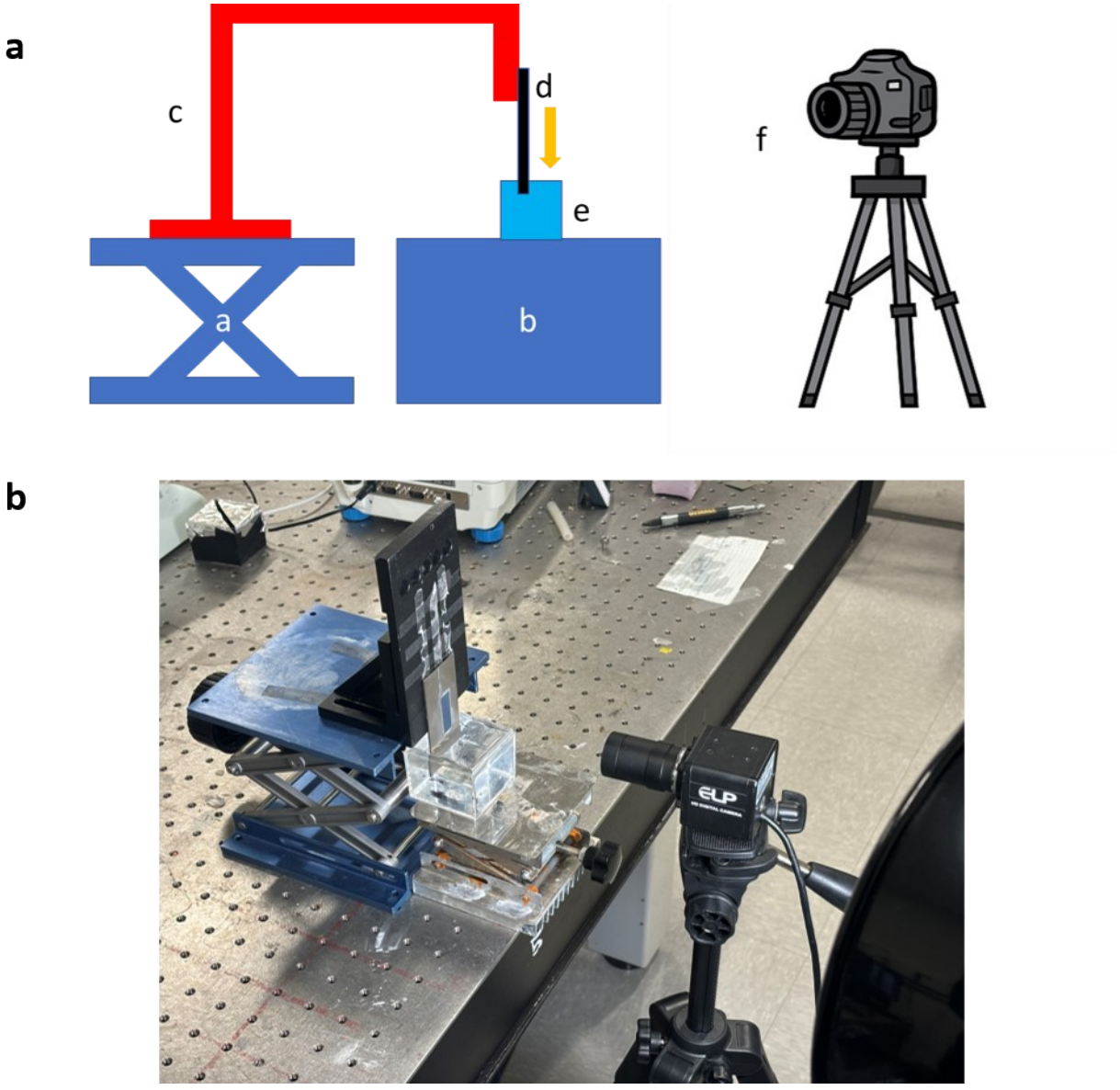

Figure S5: a) Experimental setup measuring wettability of the SWBM: a) z translation stage, b) mount, c) crane structure, d) SWBM, e) water reservoir, f) camera. The gold arrow represents the moving direction of the SWBM. b) Picture of the experimental setup. c) Snapshots of water wicking dynamics on the surface of different samples. White dashed line shows the position of the water-wet front.

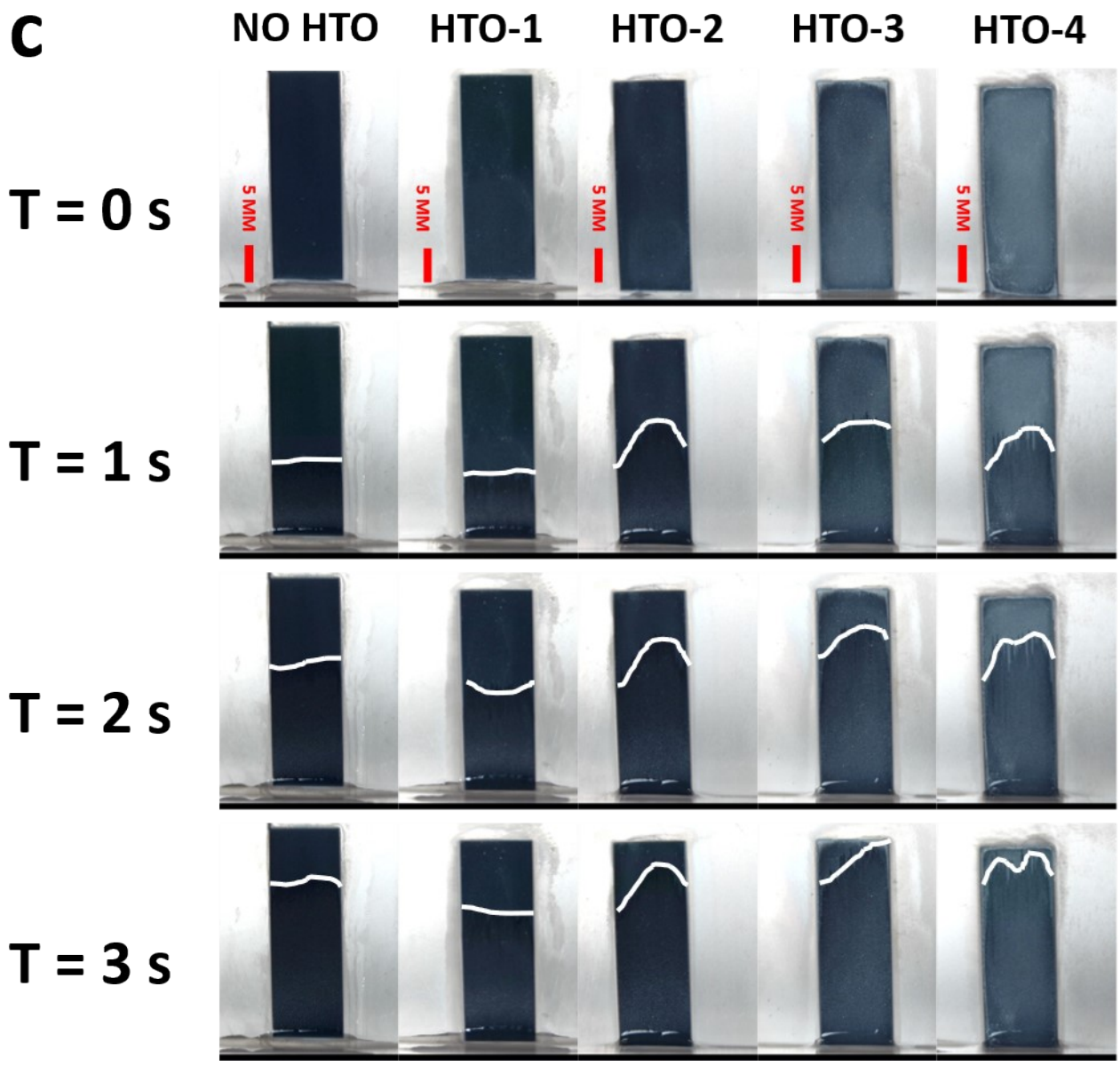
c
NO HTO
HTO-1
HTO-2
HTO-3
HTO-4
T = 0 s
T = 1 s
T = 2 s
T = 3 s
5 MM

Supplementary Note 5

Contact angle measurement of Superwicking Black Metal with and without HTO

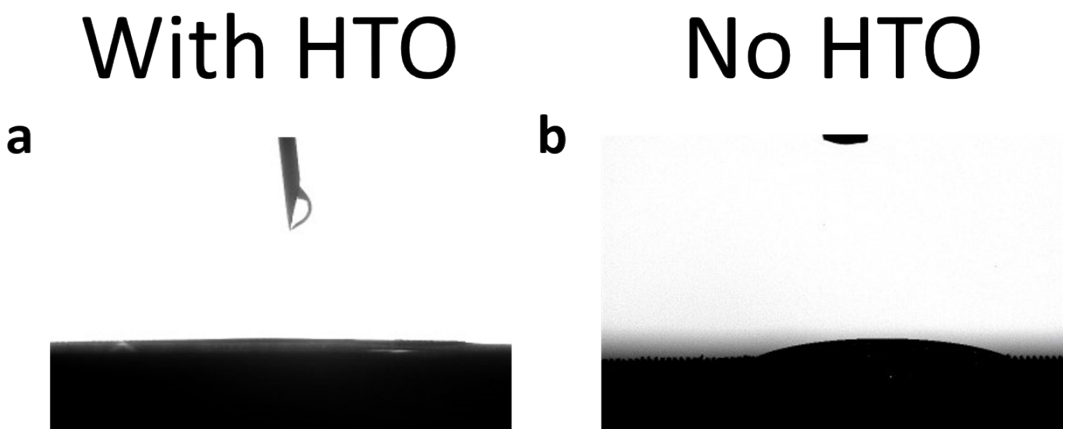

Figure S6: The contact angle of the SWBM with HTO is 1.732 degree. The contact angle of the SWBM without HTO is 19.184 degree. It turns out that HTO has good superhydrophilicity that improves the wicking property of the surface.

Supplementary Note 6

Experiment setup measuring evaporation rate

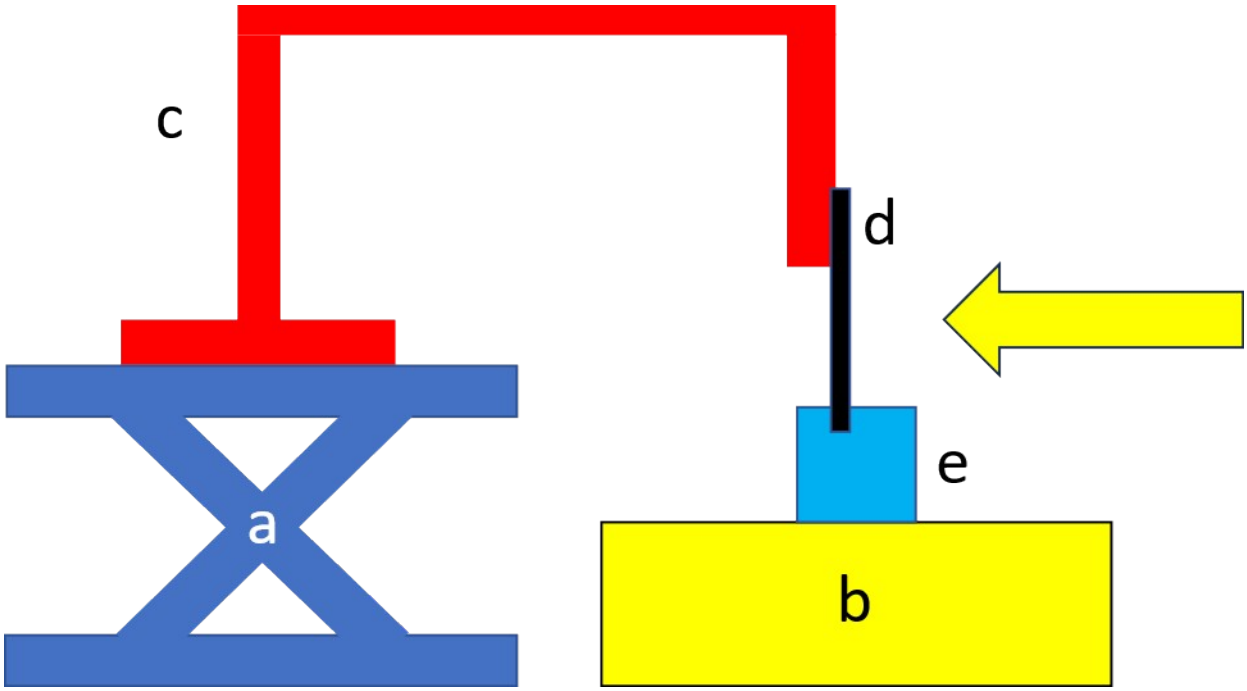

Figure S7: Experiment setup schematic diagram measuring the solar thermal evaporation rate of different sample: a) Z-translation stage, b) balance, c) jib crane structure, d) sample, e) water reservoir. The yellow arrow represents solar flux.

Supplementary Note 7

Calculation of recycle time and lithium harvest rate

The recycle time for the sample is estimated to be equal to the time when the maximum adsorption capacity of the sample is reached. Time for reaching maximum adsorption capacity is calculated by the following equation

$$T = \frac{q}{ECk_s k_a} + T_r \#(S1)$$

Where q is the maximum adsorption capacity of the sample, E is the evaporation rate of the sample, C is the concentration of the lithium ion in the solution where c=100 mg/L, ks is the factor due to solar radiation in real time operation, in this calculation, we suppose 10 hour of solar radiation of each daytime (ks=10/24), ka is the factor due to the adsorption efficiency as not all the lithium in the water evaporated is adsorbed by the HTO. In this calculation, ka=0.5. Tr is the recycle time to release the harvested lithium.

Then, the average lithium harvest rate is calculated with the following equation:

$$R = \frac{q}{T} \#(S2)$$

Where q is the maximum adsorption capacity of the sample and T is the recycle time.

Calculation of ion recover ratio

Ion recovery ratio was quantified by comparing the amount of ions collected after the experiment with the amount of ions expected to be harvested during evaporation. The ion recovery ratio, η, was calculated as

$$\eta = \frac{H}{C} \#(S3)$$

where H is the harvested ion mass and C is the ion mass theoretically associated with the evaporated water. The theoretical ion mass was calculated from

$$C = M * \rho \#(S4)$$

in which M is the mass of water evaporated and ρ is the ion concentration in the source water .The harvested ion mass H was determined from the collected products. For lithium, H was calculated from the Li concentration measured in the Li eluate by ICP-MS and the total mass of eluate collected, i.e., H = E* ρ_Li, where E is the eluate mass and ρ_Li is the Li concentration in the eluate. For the major salts (e.g., Na, K, Mg, and Ca), the precipitated solids were collected, fully dissolved in a known volume of deionized water, and the ion concentrations in the resulting solutions were measured by ICP-MS; H was then obtained by multiplying the measured concentration by the corresponding solution mass.

Supplementary Note 8

Device testing with condensation system

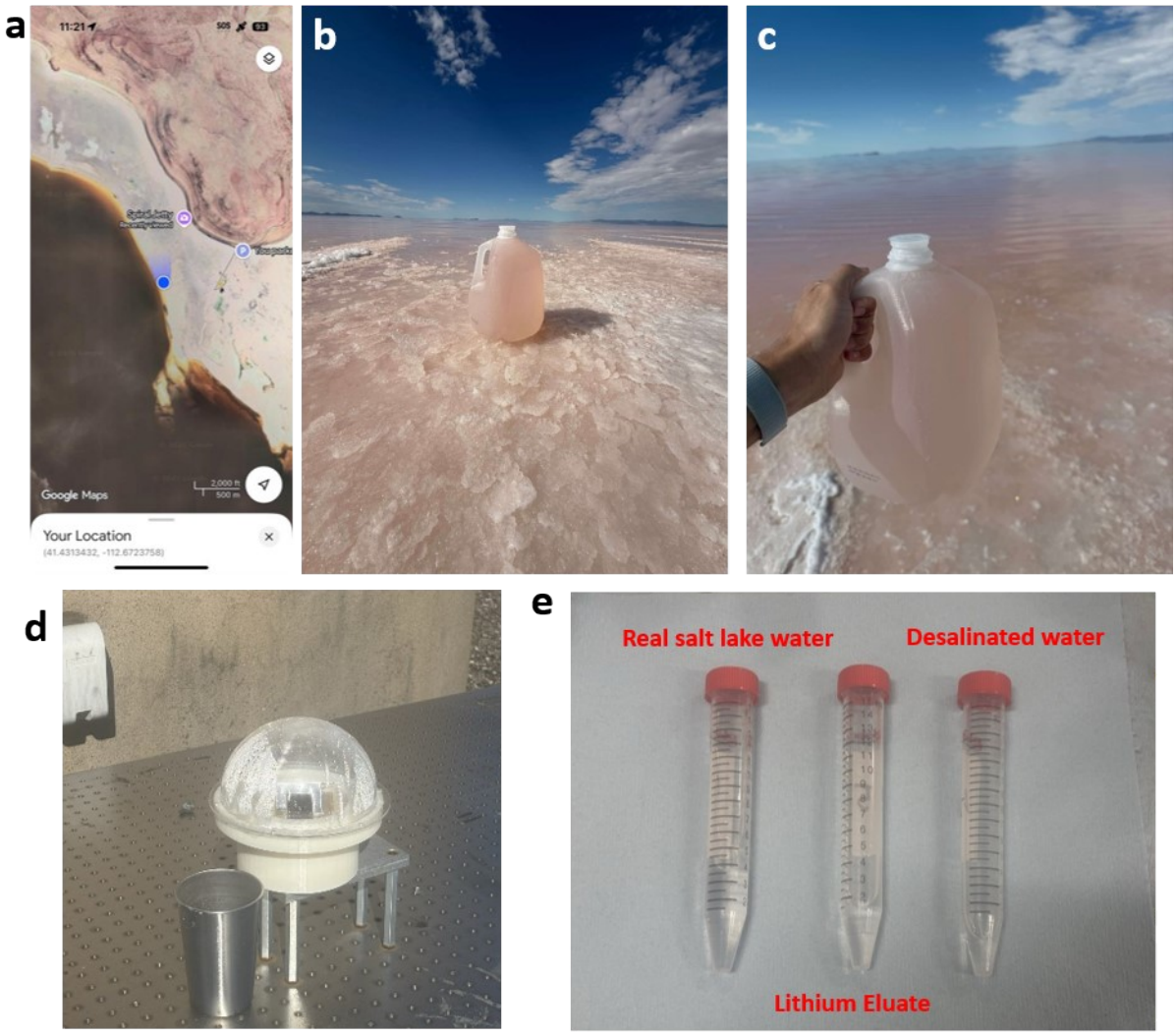

Figure S8: a) Location of the Great Salt lake water collection, b,c) Great Salt lake water collected from Spiral Jetty, UT, USA. d) Outdoor experiment setup from STEEL testing with Great Salk Lake water with a condensation system. e) Real salt lake water, Lithium eluate and Desalinated freshwater used for ICP mass measurement.

ICP-MS measurement result of tested solution

Perkin Elmer NexION 2000 Multi-element detection is used to measure the concentration of different ions in the study such as lithium, sodium, magnesium, potassium and calcium. Quantification was performed using an external calibration curve (signal intensity, counts per second) acquired under helium collision-cell (KED) conditions with a helium flow rate of 4.0 mL/min to mitigate spectral interferences. Approximately 10 mL of each solution was submitted for analysis. Each sample was measured with multiple replicate readings, and the reported concentration represents the average of the replicates.

	Real Salt Lake water (PPM)	**Lithium Eluate (PPM)**
Na	**94331.45**	**375.75**
Mg	**1098.72**	**15.03**
K	**5731.34**	**63.88**
Ca	**466.91**	**8.52**
Li	**95.63**	**1087.17**

Table S1: Cation concentration for Na, Mg, K, Ca and Li for different test solutions.

Li Selectivity estimation in this work and comparison with state-of-the-art works

The selectivity of lithium-ion adsorbents is typically defined on a molar basis as the fraction of Li^+ relative to the total cations adsorbed by the sorbent. As shown in Table S1, lithium accounts for 70.12% of the cation mass composition in the eluate, which corresponds to approximately 90.7% on a molar basis due to the low molar mass of Li^+ compared with other competing cations. Because Li^+ is expected to be released more readily than weakly adsorbed competing ions during acid elution, the molar Li fraction in the eluate represents an upper bound of the intrinsic adsorption selectivity. Accordingly, the true adsorption-based lithium selectivity of the HTO is expected to be slightly lower than the eluate molar fraction (~90%), while remaining well above the mass-based fraction. This places the intrinsic selectivity in a physically reasonable range consistent with prior HTO-based lithium-ion sieve studies (**see Table S2**) .

Reference	HTO Type	Brine Type	Li^+ Selectivity (%)
Chitrakar *et al.*, *Dalton Trans.* 2014[1]	Layered H_2TiO_3 powder	Salar de Uyuni brine	>90% of adsorbed cations
Zhao *et al.*, *RSC Adv.* 2020[2]	$H_4Ti_5O_{12}$ nanorods	Salt lake brine	~97% (Li^+ vs Mg^{2+}, Ca^{2+})
Wei *et al.*, *Chem. Eng. J.* 2020[3]	Porous HTO nanofibers	Synthetic brine	~99% (based on Kd ratios)
Sun *et al.*, *Chem. Eng. J.* 2023[4]	Nano-sized H_2TiO_3	Salt lake brine	>90% of exchanged cations
This work	HTO on STEEL surface	Real salt-lake water	70%-90% of adsorbed cations

Table S2: Li selectivity comparison with state of art work.

Economic feasibility of the system

To evaluate the economic feasibility of the system, we considered the cost of LTO nanoparticle loading and the small amount of acid required for lithium extraction. The LTO loading is 70 mg per 3 cm^2, equivalent to about 0.233 kg per m^2, and with a typical bulk price of <$100 per kilogram, the one-time material cost is approximately $23 per m^2. Each 10-day cycle requires only 50 mL of dilute HCl for recycling, which costs just a few cents per cycle. The system recovers around 76.7 g of lithium per year per m^2 considering average 10 h daylight operation each day (see Fig.3d STEEL 3), and at a representative market value of $150 per kilogram, this corresponds to an annual revenue of roughly $11–12 per m^2. Based on these values, the payback period for the nanoparticle material cost is about 2 years, demonstrating that the use of LTO does not pose a significant economic barrier and can be recovered in a relatively short time through lithium production.

Supplementary Note 9

i) Experiment layout

A two-balance experiment setup is designed to record the amount of evaporation and harvested salt simultaneously. **Figure S9** shows the diagram of the experiment setup. Two balances are mounted firmly on the table. On the left balance, there is a jib crane structure. The SWBM hangs on the hook of the jib crane structure. The bottom of the SWBM contacts the water reservoir, which is on the second balance. Note that the PPM meter is not shown in the diagram for simplification because the PPM meter is incorporated with the water reservoir.

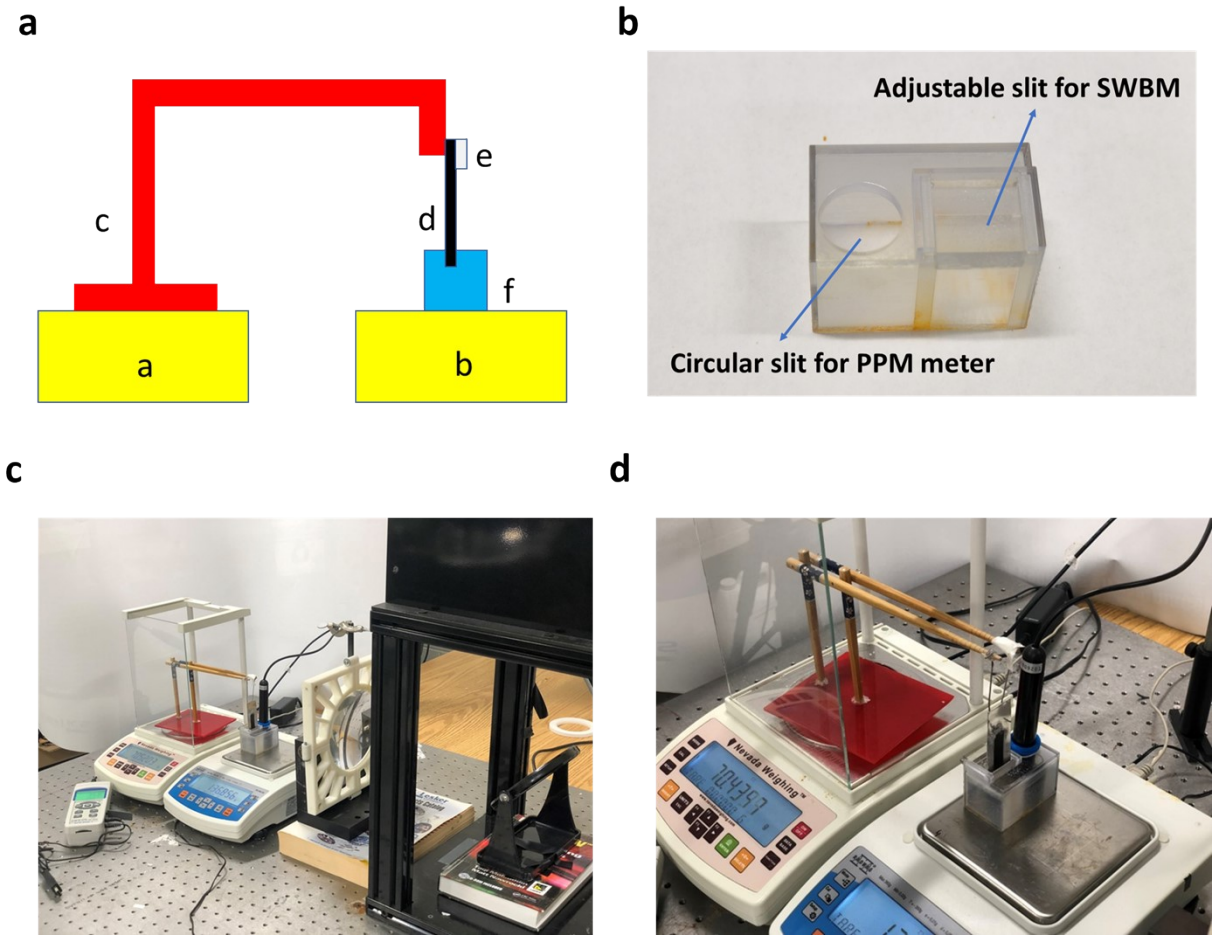

Figure S9: a) Two balance experiment setup schematic diagram: a) balance1, b) balance 2, c) jib crane structure, d) SWBM, e) salt harvested, f) water reservoir. b) 3D printed reservoir with a circular aperture to incorporate PPM meter. c) Image of two balance experiment setup. The lens could be integrated for high solar concentration conditions. d) Zoom view of two balances.

ii) Force analysis of the system

Figure S10 shows the force diagrams of the crane structure, the SWBM, and water reservoir. The force equations for these three objects are listed below:

$$F_{b1} - F_{gc} - F_{cs} = 0 \ \#(S3)$$

where F_{b1} is the normal force between balance 1 and the crane structure, F_{gc} is the gravity force of the crane structure and F_{cs} is the normal force between the crane structure and the SWBM.

$$F_{cs} + F_b - F_{ss} - F_{gs} - F_{sw} = 0 \ \#(S4)$$

where F_b is the buoyant force, F_{ss} is the friction force between the SWBM and the salt sticking on its surface. The magnitude is equivalent to the gravity force of the salt. F_{gs} is the gravity force of SWBM and F_{sw} is the hydrophilic force between the SWBM and water.

$$F_{b2} + F_{sw} - F_{gw} - F_b = 0 \ \#(S5)$$

where F_{b2} is the normal force between balance 2 and water and F_{gw} is the gravity force of water.

During the experiment time, water evaporates, and salt crystallizes on the surface of SWBM. The changing of gravity force of water and salt can be represented by the following two equations:

$$\Delta F_{gw} = \Delta m_w g \ + \Delta m_w \rho g \#(S6)$$

$$\Delta F_{ss} = - \Delta m_w \rho g \ \#(S7)$$

where Δm_w is the mass change of water due to evaporation, ρ is PPM of the water and g is gravity constant.

The water level drops because of the evaporation loss. Since this process is gradually, the system can still be regarded in a stable condition: the SWBM hangs firmly on the hook of jib crane structure and water surface is calm. Therefore, the hydrophilic force between SWBM and water doesn't change with time.

$$\Delta F_{sw} = 0 \ \#(S8)$$

Buoyant force slightly decreases because the water level drops due to the evaporation loss. The decrease of buoyant force can be calculated as:

$$\Delta F_b = \Delta m_w \frac{A_S}{A_W} g \ \#(S9)$$

where Δm_w is the mass change of water due to evaporation, A_S is the cross-section area of SWBM, A_W is the area of water reservoir.

Now, combining equations above, we can get:

$$\Delta F_{b1} = \Delta F_{ss} - \Delta F_b = - \Delta m_w \rho g - \Delta m_w \frac{A_S}{A_W} g \ \#(S10)$$

$$\Delta F_{b2} = \Delta F_{gw} + \Delta F_b = \Delta m_w g + \Delta m_w \rho g + \Delta m_w \frac{A_S}{A_W} g \ \#(S11)$$

Using $A_S = 0.02\ cm^2$, $A_w = 24\ cm^2$ and $\rho = 0.105$, we get $\frac{A_S}{A_W} : \rho = 1{:}126$, Thus, the change of buoyant force is negligible compared with the change of gravity force of water and salt. We can assume:
$\Delta F_b = 0\ \#(S12)$

Finally, we can get:
$\Delta F_{b1} = \Delta F_{ss} = -\Delta m_w \rho g\ \#(S13)$
$\Delta F_{b2} = -\Delta F_{gw} = \Delta m_w g\ + \Delta m_w \rho g \#(S14)$

The result shows that the change of mass reading on balance 1 represents the accumulation of salt on the SWBM surface and the change of mass reading on balance 2 represents the loss of water and mineral in the reservoir due to evaporation.

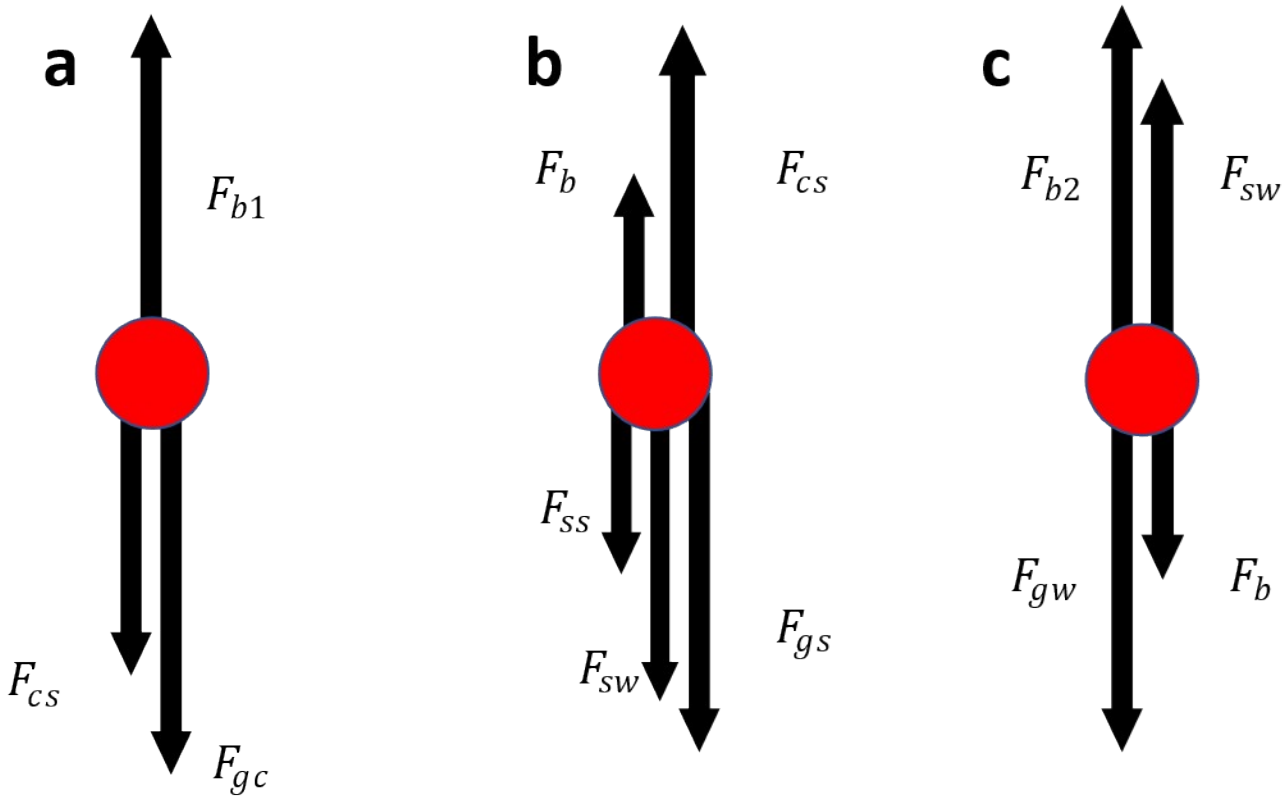

Figure S10: Force diagram of a) the crane structure, b) the SWBM, c) water reservoir

Surface self-cleaning and harvested salt EDAX

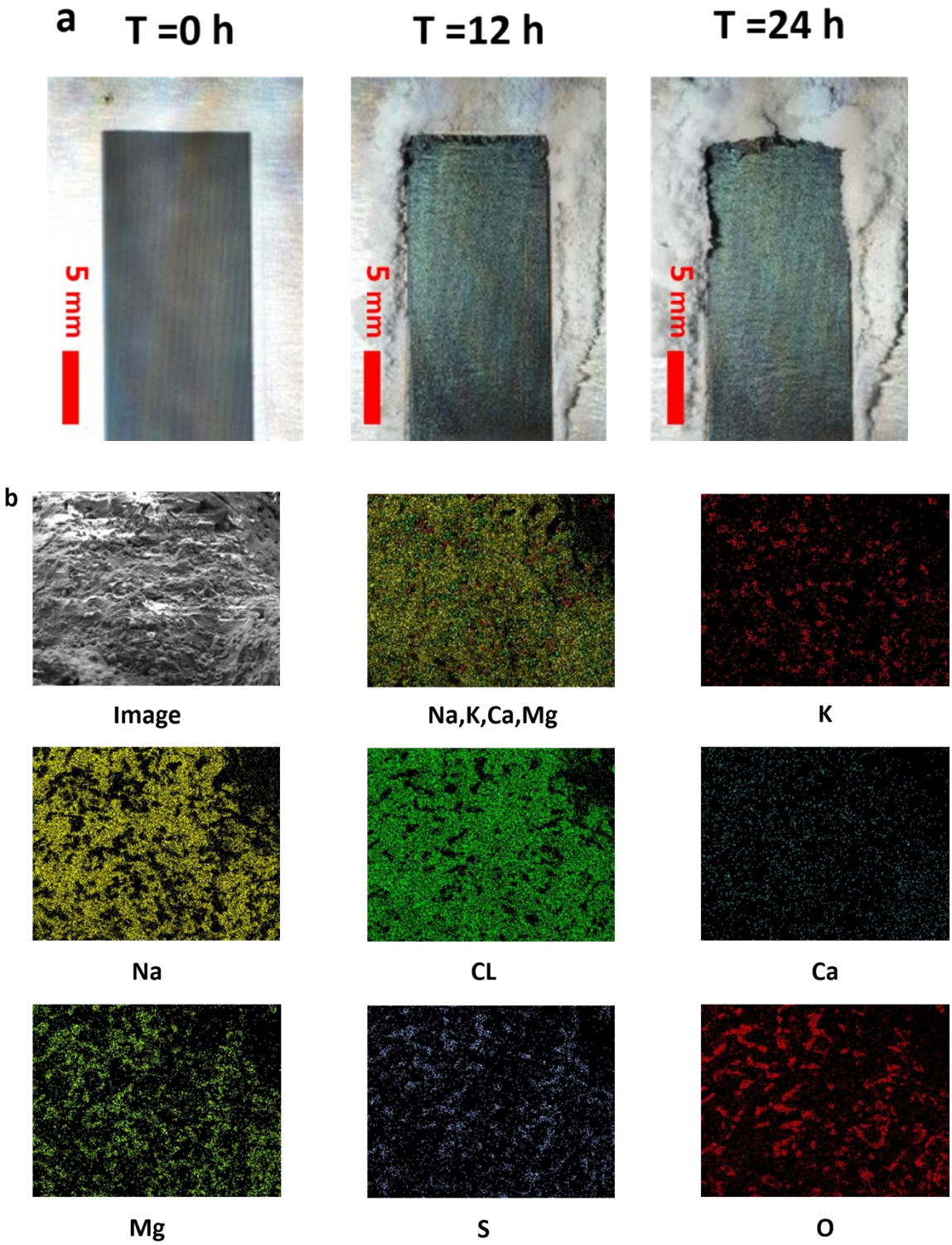

Morphological and compositional comparison

Figure S11c compares the microscope image of the HTO particles for the first cycle and after 25 cycle. No distinct morphological change is observed indicating durability of HTO particles. Additionally, XRD analysis for the two cases are compared. The peak at 46 and 66 deg all disappear which indicates no chemical compositional change.

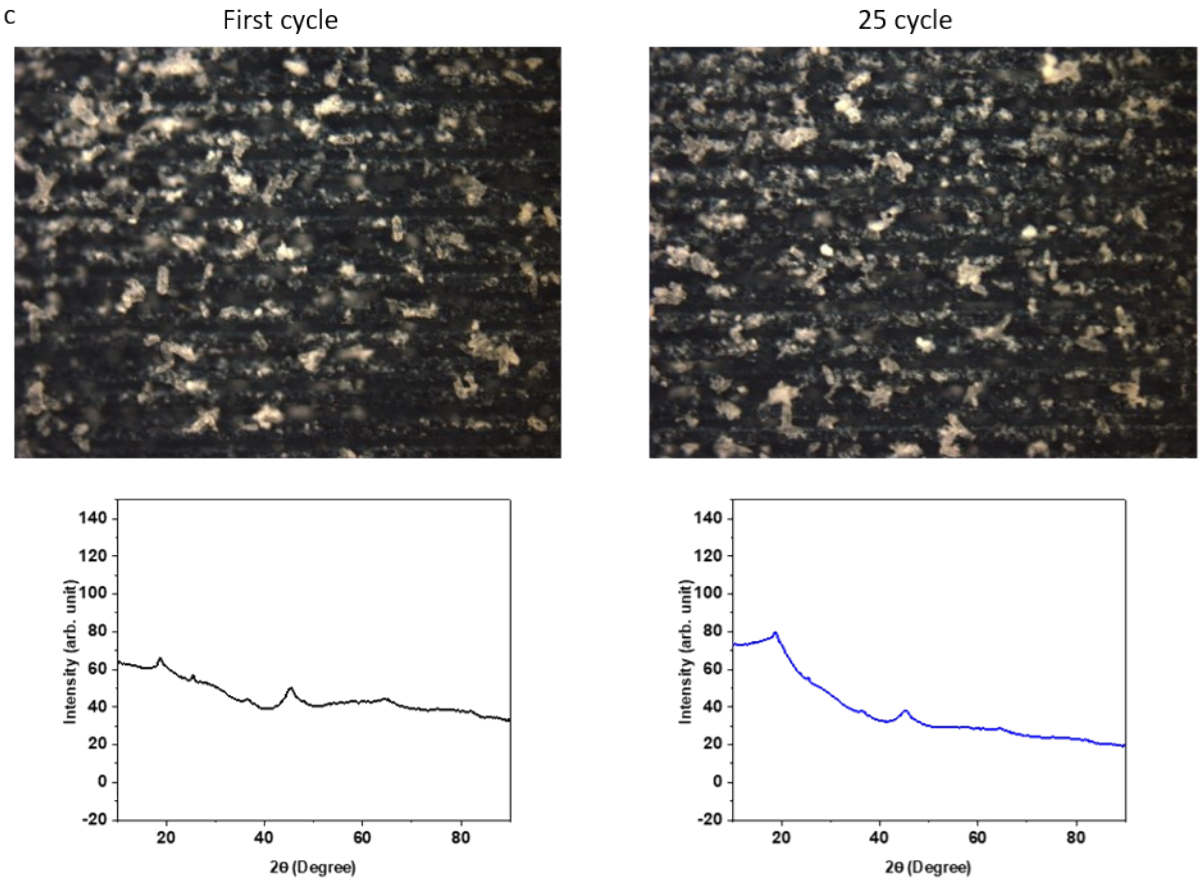

Figure S11: a) Snap shots of STEEL-3 sample during solar thermal interfacial desalination when treating simulate the Great Salt Lake water under one sun illumination. The time step between each photo is 12 hours. The first image shows the initial moment when the SWBM's bottom just touches water. We consider the SWBM surface that absorbs light and wicks water as the active region while the surrounding region as the passive region. The active region wicks the water uphill and spread it to the surrounding passive region. As time goes on, salt will start to crystallize at the edges of water boundary in the passive region and grow outwards. As a result, no salt crystal is observed in the active region and all the salt crystals are harvested on the passive region. This salt growing pattern can be explained by the combination of two physics theories: coffee ring effect followed by salt creeping. b) EDAX elemental mapping of the salt harvested with image and mapping of Na, K, Cl, Ca, Mg, S and O. c) microscope and XRD comparison for STEEL for the first cycle and 25 cycle.

Supplementary Note 11

Mineral mining and self-cleaning dynamics

Observation of salt growth using microscope

Due to the vertical orientation of the microscope objectives, it is not feasible to directly observe the salt growth patterns when the SWBM is mounted vertically. Therefore, an altered configuration, as depicted in **Figure. S12a**, is employed. In this setup, the SWBM is placed horizontally on the microscope's platform. Adjacent to the microscope, a solar simulator is installed at an angle, with its power adjusted to produce irradiance equivalent to one sun. Seawater is consistently introduced from the bottom of the SWBM using a syringe. This arrangement replicates the experimental conditions as closely as possible, allowing us to observe the salt growth phenomenon, which can subsequently be applied to experimental scenarios.

Thin film solution wicking on salt crystals

The thin film solution wicking on salt crystals is directly observed using light microscope. Firstly, seawater is supplied from the bottom of the SWBM and waits for natural drying. Sea salt crystals will form on the passive area due to the coffee ring effect. **Fig. S12b** shows the sea salt crystals on the passive area in dry condition. Subsequently, seawater is reintroduced, and as shown in **Figure. S12c**, the image becomes defocused, indicating that the salt crystals are covered by the thin film solution.

Water transportation through pores of salt crystal

Sea salt primarily comprises sodium chloride, whose crystal structure is cubic [5]. The presence of imperfections in the arrangement of these cubic crystals results in the formation of tiny gaps between them, rendering sea salt porous. Consequently, thin film solution can permeate through these crystals and travel within their pores, as illustrated in **Figure. S12d**. In this figure, the grey cubes signify the salt crystals, while the blue arrow signifies the movement of water. As a consequence of this water movement, a thin layer of liquid forms on the surface of these crystals. Subsequently, water evaporates rapidly from the surface of these crystals, as depicted in **Figure. S12e**. Consequently, the overall rate of evaporation increases.

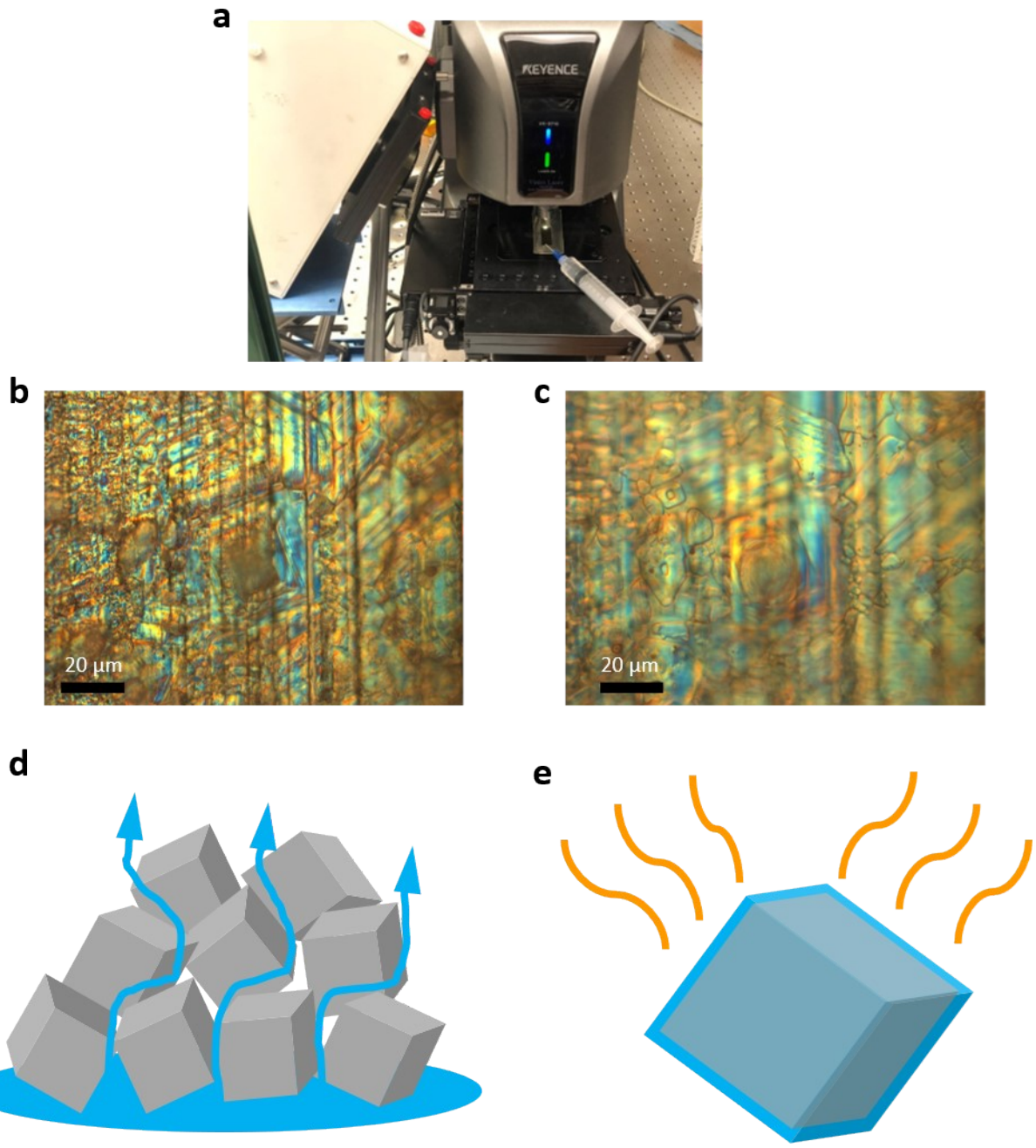

Figure S12: a) Experiment setup observing salt growth using light microscope, b) Salt crystal on the passive area in dry condition. c) Salt crystal covered by the thin film solution when water is supplied. d) Water transportation through pores of sea salt. e) Thin film forms on the salt crystal and boosts evaporation.

Supplementary Note 12

Salt solution concentration distribution along the capillary

A physics-based model is utilized to approximate the concentration distribution of the solution throughout the capillary. Only one capillary is examined assuming the uniformity of all capillaries in the SWBM. The distribution of concentration along the capillary is illustrated by a 101 x 1 matrix, where each element in the matrix represents the average concentration of an area. The first element denotes the passive region on the top, while the remaining 100 elements signify the capillary. Initially, the concentration of each element is equal to that of the water reservoir. Then, the concentration change for each unit is computed after every time step, which is 0.1 seconds. The concentration change is evaluated by considering several processes such as evaporation, dilution, ion diffusion, crystallization, and dissolution. **Figure. S13a** depicts the flow chart of how the concentration change is calculated. To simplify the calculation, several assumptions are made.

1) The rate of evaporation is the same everywhere in the capillary.
2) The evaporation loss is balanced by the upward capillary flow quickly so that the volume of water in the capillary doesn't change.
3) The capillary shape profile is uniform along the capillary so that the volume of each unit is the same.
4) The coefficient of ion diffusion and dissolution is the same everywhere.
5) Salt participates quickly as long as concentration is larger than saturation.

Details of how each mechanism change concentration values are shown below:

Evaporation:

$$C_i = \begin{cases} \dfrac{C_i \times V}{V - bkt} & (i = 1) \\ \dfrac{C_i \times V}{V - kt} & (else) \end{cases} \#(s16)$$

Dilution:

$$C_i = \begin{cases} \dfrac{C_i \times (V - (i+b)kt) + C_w \times (i+b)kt}{V} & (i = 101) \\ \dfrac{C_i \times (V - (i+b)kt) + C_{i+1} \times (i+b)kt}{V} & (else) \end{cases} \#(s17)$$

Ion diffusion[6]:

$$C_i = \begin{cases} \dfrac{[C_i \times V - \dfrac{(C_i - C_{i-1})}{L} \times k_i t]}{V} & (i = 1) \\ \dfrac{[C_i \times V - \dfrac{(2C_i - C_w - C_{i-1})}{L} \times k_i t]}{V} & (i = 101) \\ \dfrac{[C_i \times V - \dfrac{(2C_i - C_{i+1} - C_{i-1})}{L} \times k_i t]}{V} & (else) \end{cases} \quad \#(s18)$$

Crystallization:

$$if\ C_i \geq C_s,\ then \begin{cases} C_i = C_s \\ P_i = P_i + (C_i - C_s) \times Vt \end{cases} \quad \#(s19)$$

Dissolution[7]:

$$if\ P_{i-1} \geq 0,\ then \begin{cases} C_i = \dfrac{C_i \times V + \dfrac{(C_s - C_i)}{C_s} \times k_d t}{V} \\ P_{i-1} = P_{i-1} - \dfrac{(C_s - C_i)}{C_s} \times k_d t \end{cases} \quad \#(s20)$$

where C_i is the concentration in ith unit, C_w is the concentration of water reservoir, C_s is the saturation concentration of water reservoir, V is the volume of each unit, L is the length of each unit, t is time step, b is the scaling factor for passive area, S is the cross section area of the capillary, k is the rate of evaporation, k_i is the rate of ion diffusion in capillary, k_d is the rate of dissolving and P_i is the volume of crystallization in ith unit.

Figure. S13b displays the stable concentration distribution. The concentration exhibits an exponential distribution along the capillary. In stable condition, only the first unit's concentration becomes higher than saturation, which means salt only crystallized on the passive area. The concentration close to the water reservoir has nearly the same concentration as the water reservoir. Therefore, the ion diffusion back to the water reservoir is negligible and all the ions finally crystallized on the passive area.

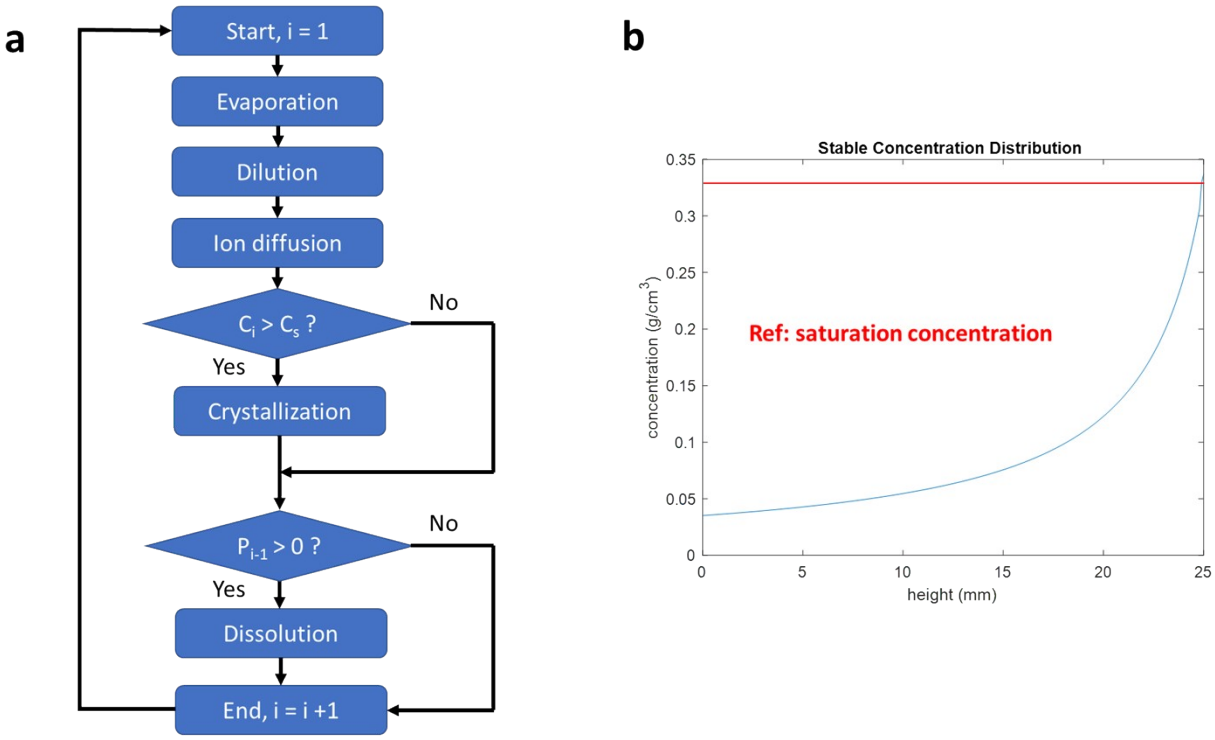

Figure S13: a) Flow chart of the calculation, b) Simulation result of stable concentration distribution along the capillary.

Florescence imaging measuring the concentration gradient along the capillary

Direct measurement of the concentration of salt water in the capillary is challenging due to the micro-scale dimension of the water in the capillary. To address this issue, Florescence imaging (Keyence BZ-X800 Epifluorence Microscope) is used to measure the concentration distribution along the capillary of SWBM. **Figure S14a** shows the experiment setup. Water with Rhodamine 6G (R6G) is constantly added at one end of SWBM (reservoir) and wicks its surface. R6G particles emit signal which is then collected by the objective below. The objective moves around to capture florescence images at different locations of the SWBM. The concentration of the R6G can be examined by looking at the distribution of the signal. Note that R6G is a water-soluble dye which behaves the same as the salt. Therefore, the concentration distribution of R6G inside the capillary is equivalent to the concentration distribution of the salt. Figure S24b is the stitched fluorescence image showing the concentration distribution of R6G over the SWBM. The concentration of R6G is low at the region close to the reservoir and high at the region away from the reservoir. The concentration along the capillary direction follows an exponential increase with the distance away from the reservoir (Figure S24c). Some much brighter spots on the passive region corresponds to the saturation concentration (crystallization) on the passive region. Therefore, the concentration of the solution exponentially increases along the capillary length and saturation concentration happens only at the passive region.

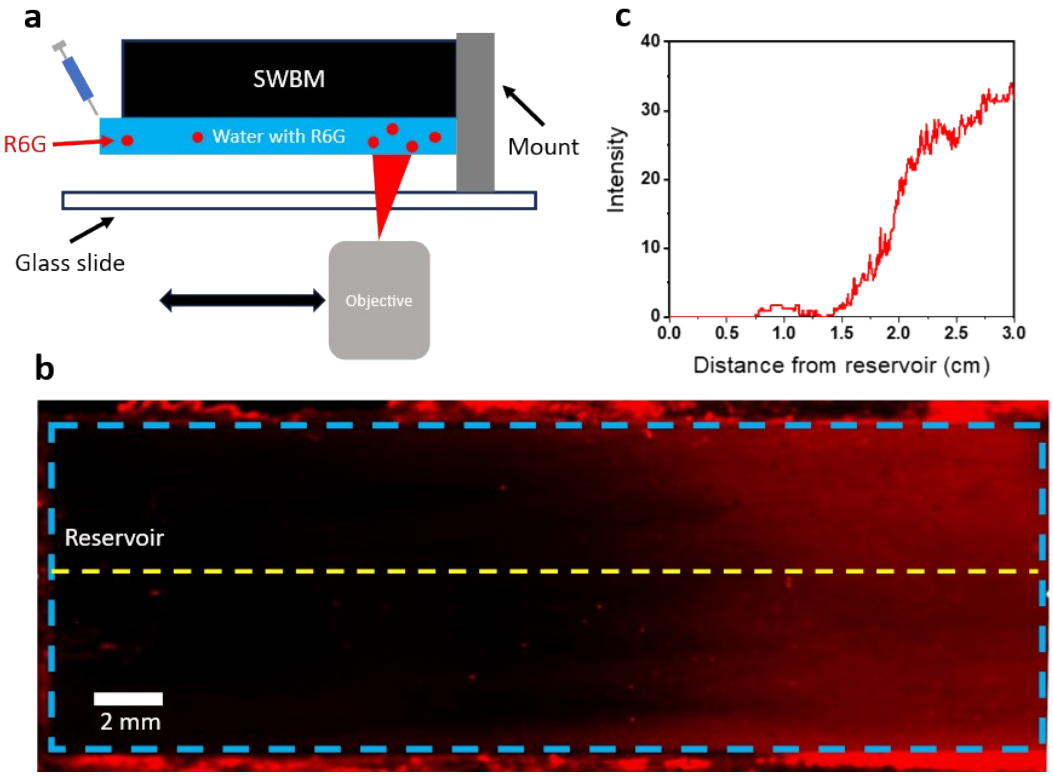

Figure S14: a) Florescence imaging setup using R6G. b) Fluorescence image of the SWBM. Blue dash line marks the active region of the SWBM, and yellow line marks the line for intensity analysis. c) R6G florescence signal intensity distribution along the capillary.

Supplementary Note 13

Modeling Salt Concentration Dynamics in evaporating and crystallizing region

This note presents a modeling framework for simulating the evolution of salt concentration in evaporating (active) and crystallizing (passive) regions. Each region is characterized by a fixed volume: Ve (evaporating) and Vc (crystallizing). Evaporation occurs at rates Ke and Kc (in volume per time) in the evaporating and crystallizing regions, respectively. The reservoir supplies fluid of initial concentration C_0. Due to coffee ring effect, we assume evaporation happens only at the edge of the crystallizing region. Water evaporates at the edge and leaves crystallized salt on the edge. We suppose the evaporate rate in evaporating is uniform all over space and water loss due to evaporation is quickly refilled due to strong wicking effect of the evaporating region. Therefore, the concentration profile along evaporating region is exponential (**see Supplementary Note 12**). To describe this exponential gradient, we define the interface concentration at the edge of the evaporating region adjacent to the crystallizing region as Cec, and its relationship with reservoir concentration and average evaporating concentration is defined as follow:

$$C_{ec} = (1 + a)C_e - aC_0 \#(s21)$$

where a is a prescribed slope parameter representing exponential concentration gradient across the evaporating region. Additionally, we define b as the ratio of boundary water volume to bulk water volume in the crystallizing region.

Dynamic Evolution Equations

We define a unit time step as the time required for all the water at boundary evaporates. In each time step Δt, the following updates are performed:

1. Evaporation-induced concentration in the evaporating region:

$$C_e^{'} = \frac{C_e V_e}{V_e - K_e \Delta t} \#(s22)$$

2. Concentration in the crystallizing region after crystallization and inflow from the interface:

$$C_c^{'} = \frac{C_c(V_c - K_c \Delta t) + C_{ec} K_c \Delta t}{V_c} \#(s23)$$

3. Concentration in the evaporating region after receiving reservoir fluid and losing salt to interface:

$$C_e^{''} = \frac{C_e^{'}(V_e - K_e \Delta t) - C_{ec} K_c \Delta t + C_0(K_e + K_c)\Delta t}{V_e} \#(s24)$$

Steady-State Analysis

At steady state, we assume Cc' = Cc and Ce'' = Ce. Begin with Eq. (s23). Solving for Cc in steady state:

$$C_c = C_{ec} \#(s25)$$

Substitute Eq. (1) into Eq. (s20):

$$C_c = (1 + a)C_e - aC_0 \#(s26)$$

Now substitute $C_{ec} = C_c$ into the steady-state form of Eq. (s24):

$$C_e = \frac{C_e V_e - C_c K_c \Delta t + C_0 (K_e + K_c)\Delta t}{V_e} \#(s27)$$

Rewriting and simplifying:

$$C_c = \frac{(K_e + K_c)}{K_c} C_0 \#(s28)$$

Then plug Eq. (s23) into Eq. (s21) to find Ca:

$$C_c = \frac{K_c + K_e + aK_e}{(1 + a)K_c} C_0 \#(s29)$$

Requirement for surface self-cleaning when treating NaCl only water

To continuously edgewise crystallization when treating NaCl only water, the only requirement letting the concentration of solution in crystallizing region below than the saturation concentration because NaCl crystals are porous and water can wick thorough the NaCl crystals to enable outward crystallization expansion. Therefore:

$$K_e < \left(\frac{C_{sat}}{C_0} - 1\right) K_c \#(s30)$$

Requirement for salt-lake water self-cleaning evaporator

To model the dissolution of solid NaCl into undersaturated water, we consider a one-dimensional, diffusion-limited process where a flat salt–solution interface recedes as salt dissolves into a stagnant liquid phase. The system is analogous to a classical Stefan problem describing phase change (e.g., melting or evaporation), but here applied to dissolution.

Let C(x,t) be the concentration of dissolved NaCl in the liquid phase, with x denoting the distance from the solid–liquid interface and t the time. Assuming only molecular diffusion contributes to transport (i.e., neglecting convection and activity effects), the solute transport is governed by Fick's second law:

$$\frac{\partial C}{\partial t} = D \frac{\partial^2 C}{\partial x^2}, \quad for\ 0 < x < d(t) \#(s31)$$

where D is the diffusivity of NaCl in water (cm^2/s), and L(t) is the position of the moving dissolution front.

We assume the following boundary and initial conditions:
Initial condition: C(x,0) = Ce for x > 0
Interface condition: C(L(t),t) = C_{sat}

At the dissolving interface, the recession of the salt surface is governed by mass conservation:

$$\rho \frac{dL}{dt} = -D \frac{\partial C}{\partial x}\Big|_{(x = d(t))} \#(s32)$$

We assume a similarity solution of the form C(x,t) = f(η), where $\eta = \frac{x}{2\sqrt{Dt}}$. This yields a moving front position of the form $d(t) = 2\lambda\sqrt{Dt}$, where λ is a dimensionless constant determined by boundary conditions.
Solving the resulting ODE yields the concentration profile:

$$C(x,t) = C_e + (C_{sat} - C_0)\frac{\mathrm{erf}\left(\frac{x}{2\sqrt{Dt}}\right)}{\mathrm{erf}(\lambda)} \#(s33)$$

From this, the gradient at the interface is substituted into the interface condition to yield a transcendental equation for λ.

$$\lambda e^{\lambda^2} \operatorname{erf}(\lambda) = \frac{(C_{sat} - C_e)}{\rho_s} \#(s34)$$

For practical purposes, an approximate analytical solution is used:

$$d(t) \approx 2\sqrt{\frac{D\,(C_{sat} - C_e)t}{\pi\,\rho_s}} \#(s35)$$

When NaCl crystallizes, it tends to be cubic form. Therefore, we approximated the crystallized NaCl is the form of a rectangular cuboid where width and height are the same. At given t, the width of the NaCl cuboid can be expressed as:

$$w(t) = \sqrt{\frac{\rho_w k_c\, C_e t}{\varepsilon \rho_s}} \#(s36)$$

where kc is the evaporation rate per unit length at the boundary , C is the concentration of NaCl in seawater, ε is the porosity of NaCl crystals.

When treating salt-lake water, $MgSO_4$ might block the pores for the NaCl crystal, therefore, the solution needs to dissolve the NaCl to provide additional path to let water wick through. To achieve this, the dissolution length needs to be larger than several times width of the NaCl cuboid:

$$d(t) > \alpha w(t) \#(s37)$$

Using equations s35 and s36, we get:

$$C_e < \frac{C_{sat}}{\left(\frac{\alpha^2 \pi \rho_w k_c}{4D\varepsilon} + 1\right)} \#(s38)$$

From previous model,

$$C_e = \frac{(K_e + K_c)}{K_c} C_0 \#(s39)$$

Combing equations s38 and s39, we get the requirement for self-cleaning:

$$K_e < K_c\left(\frac{C_{sat}}{C_0\left(\frac{\alpha^2 \pi \rho_w k_c}{4D\varepsilon} + 1\right)} - 1\right) \#(s40)$$

Self-cleaning for STEEL

To determine the evaporation mass flux contribution from the evaporating and crystallizing regions, we performed comparative experiments using STEEL with untreated crystallizing region and crystallizing region inhibited case. In the crystallizing region inhibited case, the hydrophobic paint is added on the edge of the evaporator which traps water film within the microcapillaries. As shown in **Figure S15a**, water wicks along the capillaries but is pinned at their edges and does not propagate onto the surrounding untreated surface. The hydrophobic paint acts as a barrier, preventing further lateral wicking. **Figure S15b** presents the measured water film profile in this inhibited configuration. On the untreated region, the surface height with and without water is nearly identical, confirming no water coverage. At the microcapillary edge, a ~30 μm thick hydrophobic layer is clearly observed, while the water film thickness in the central (bulk) capillary region exceeds 200 μm. All the water remains confined within the evaporating region, and no thin-film evaporation (<30 μm) is observed in the crystallizing zone. Therefore, in this case, all evaporation originates exclusively from the evaporating region with no contribution from the crystallizing region. **Figure S15c** shows the evaporation mass flux verse time for STEEL with and without crystallizing region. The red line represents the contribution from crystallizing region while the green line represents the contribution from the evaporating region. From the result, $\boldsymbol{K_e}$ = 0.72 kg/m^2/h while $\boldsymbol{K_c}$ = 0.33 kg/m^2/h, $\left(\frac{C_{sat}}{C_0\left(\frac{\alpha^2\pi\rho_w k_c}{4D\varepsilon}+1\right)}-1\right)\approx 3$, therefore, Equation S40 is satisfied. For most porous materials without crystallizing region, the salt crystal itself acts like the crystallizing region. However, the salt crystals lacks enough space for thin-film evaporation which $\boldsymbol{K_c}$ small ~0.1 kg/m^2/h. As a result, most porous material system even open capillary-based water transport system (**Figure. S15d**) suffers capillary clogging issue.

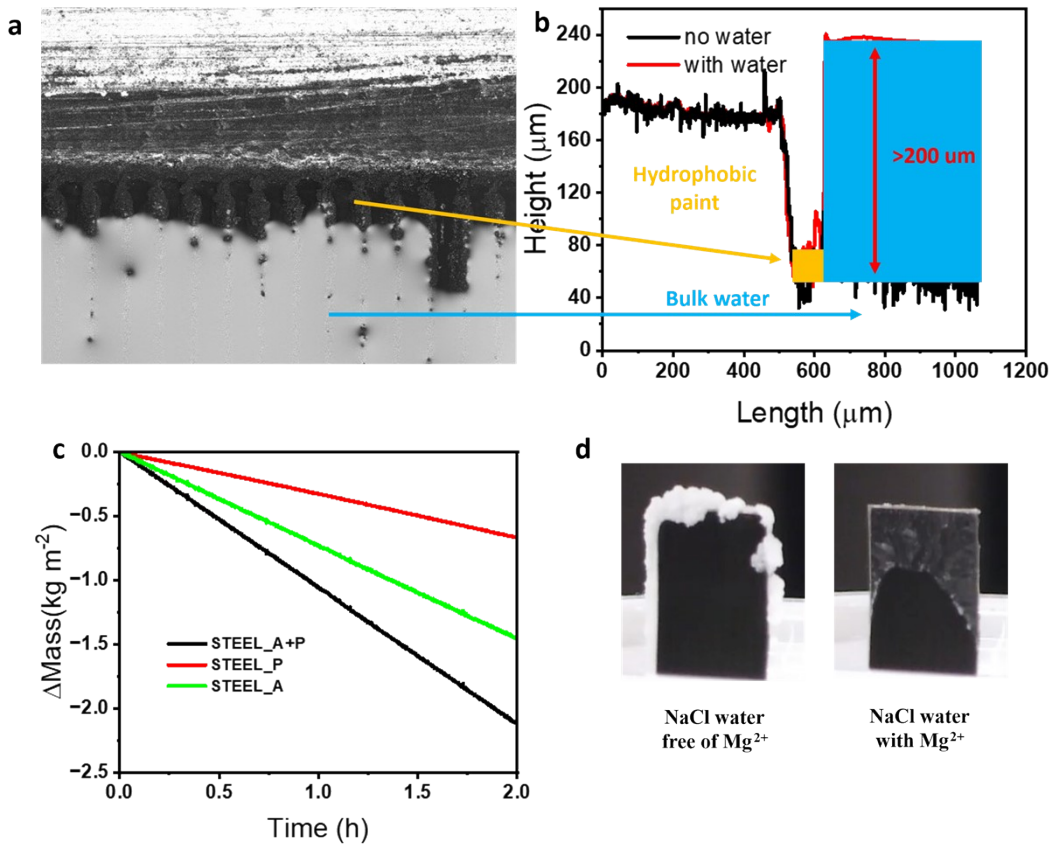

Figure S15: a) Image of water film profile for crystallizing region inhibit case. b) Water film profile for crystallizing region inhibited case. c) Evaporation mass flux verse time for STEEL with and without crystallizing region. d) Comparing open capillary wicking material when treating Mg removed water vs. Mg containing water under 1 sun after 4 hours. While the surface remains clean when treating Mg removed water, scaling and clogging are obvious when treating Mg containing water.

Supplementary Note 14

Salt accumulation on an open capillary surface that is not designed for self-cleaning

A control experiment is performed to compare the long-term evaporation performance of a porous fiber coated with black paint (**as shown in Fig. S16**) under solar radiation. For the porous material surface, the evaporation rate is recorded when treating real oceanwater under 1 sun illumination. The surface was heavily covered by salt crystals due to capillary clogging, leading to a significant drop in evaporation rate (**Fig S16**).

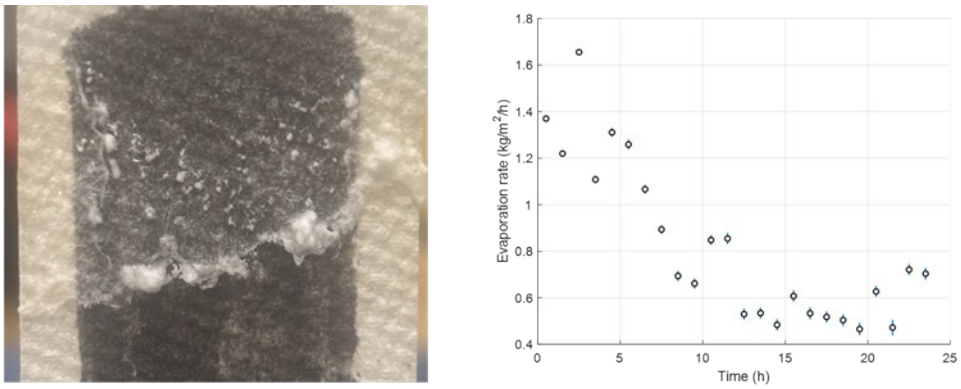

Figure S16: left) Accumulation of salt on the active area of porous material, right) the evaporation rate of the porous material under 1 sun illumination during 24 hour period, the rate drops significantly due to clogging.

Reference:

1. Chitrakar, R., Y. Makita, K. Ooi, and A. Sonoda, *Lithium recovery from salt lake brine by H2TiO3.* Dalton Trans, 2014. **43**(23): p. 8933-9.
2. Zhao, B., et al., *Hydrothermal synthesis and adsorption behavior of H(4)Ti(5)O(12) nanorods along [100] as lithium ion-sieves.* RSC Adv, 2020. **10**(58): p. 35153-35163.
3. Wei, S., et al., *Porous lithium ion sieves nanofibers: General synthesis strategy and highly selective recovery of lithium from brine water.* Chemical Engineering Journal, 2020. **379**.
4. Sun, J., et al., *Preparation of high hydrophilic H2TiO3 ion sieve for lithium recovery from liquid lithium resources.* Chemical Engineering Journal, 2023. **453**.
5. Gibbs, W.E. and W. Clayton, *The Production of Large, Clear, Cubical Crystals of Sodium Chloride.* Nature, 1924. **113**(2840): p. 492-493.
6. Yong, Y., et al., *Direct simulation of the influence of the pore structure on the diffusion process in porous media.* Computers & Mathematics with Applications, 2014. **67**(2): p. 412-423.
7. Simon, B., *Dissolution rates of NaCl and KCl in aqueous solution.* Journal of Crystal Growth, 1981. **52**: p. 789-794.